

Probing Topological Anderson Transition in Quasiperiodic Photonic Lattices via Chiral Displacement and Wavelength Tuning

Abhinav Sinha,¹ Trideb Shit,¹ Avinash Tatarwal,¹ Diptiman Sen,² and Seabrat Mukherjee^{1,*}

¹*Department of Physics, Indian Institute of Science, Bangalore 560012, India*

²*Centre for High Energy Physics, Indian Institute of Science, Bangalore 560012, India*

The interplay of topology and disorder in quantum dynamics has recently attracted significant attention across diverse platforms, including solid-state devices, ultracold atoms, and photonic systems. Here, we report on a topological Anderson transition caused by quasiperiodic inter-cell coupling disorder in photonic Su-Schrieffer-Heeger lattices. As the quasiperiodic strength is varied, the system exhibits a reentrant transition from a trivial phase to a topological phase and back to a trivial phase. Unlike the traditional detection of photonic topological edge modes, we measure the mean chiral displacement from the transport of light in the bulk of the lattices. In our photonic lattices with a fixed length, the propagation dynamics is retrieved by varying the wavelength of light, which tunes the inter-waveguide couplings.

Introduction.— Topological materials exhibit remarkable robustness against defects, disorders, and imperfections [1–4]. This topological robustness is usually destroyed by strong disorder, which drives a topologically non-trivial system into a trivial one. Interestingly, disorder can also transform a trivial system into a topological one [5–7]. The interplay of disorder and topology has opened exciting avenues, leading to the observation of disorder-induced topological materials, known as topological Anderson insulators (TAIs) [5, 6]. The phenomenon was first predicted in HgTe quantum wells in the context of the quantum spin Hall effect, where strong disorder resulted in quantized conductance in an otherwise trivial system in the clean limit [5]. Since then, disorder-induced topology has been extensively studied, with numerical and experimental investigations exploring its underlying mechanisms [8–16].

Artificial systems, like photonic lattices and ultra-cold atoms, provide an excellent experimental platform for exploring a broad range of transport and localization phenomena [17–19]. These lattices enable precise engineering of coupling strengths and geometries, facilitating the realization of diverse Hamiltonians. Their design flexibility, tunability, and the ability to directly visualize the evolution of an initial state make them ideal for studying topological transitions and measuring invariants in complex systems. Recently, TAIs have been realized in two-dimensional Floquet photonic networks [20] and in one-dimensional bipartite cold-atomic systems [21] with uncorrelated random disorder. Using one-dimensional coupled photonic resonators [22], *gapped* and *ungapped* TAI phases have been demonstrated, where zero-energy topological edge states appear in a band gap and within bulk bands, respectively.

Unlike systems with random disorder [23–25], quasiperiodic lattices [26–31] with deterministic disorder exhibit intriguing localization transitions in low dimensions. The effects of different types of disorder

on topological phases [32–36] and on topological phase boundaries constitute an active field of research. Notably, a single topological transition from a trivial to an ungapped non-trivial phase has been reported in one-dimensional quasiperiodic photonic circuits [37–39], by detecting the presence of zero-energy modes.

In this work, we measure the bulk topological invariant to demonstrate a *reentrant* topological transition from a trivial phase to a gapped TAI and back to trivial in quasiperiodic Su-Schrieffer-Heeger (SSH) photonic lattices. To this end, we realize femtosecond laser-fabricated [40, 41] SSH lattices and measure the mean chiral displacement [42–46] from the output intensities in the bulk of the lattices to quantify the topological invariant. We employ a wavelength-tuning technique, which enables us to vary the normalized propagation distance by tuning the inter-waveguide couplings. The accuracy of the wavelength tuning is first validated by observing a topological phase transition in ‘clean’ SSH lattices. By measuring the variation of the mean chiral displacement with quasiperiodic strength, we then observe the reentrant topological Anderson transition. We also show that the topological phase diagram is independent of the specific irrational number used to realize quasiperiodicity.

Model.— In our study, we consider a one-dimensional quasiperiodic model described by the tight-binding Hamiltonian

$$\hat{H} = - \sum (J_{1,n} \hat{a}_n^\dagger \hat{b}_n + J_{2,n} \hat{b}_n^\dagger \hat{a}_{n+1} + \text{H.c.}), \quad (1)$$

where \hat{a}_n, \hat{b}_n are annihilation operators for the two sites (A and B) of the n -th unit cell, as shown in Fig. 1(a). The intercell coupling $J_{1,n} = J_1(1 + \xi \cos(2\pi\alpha n + \phi))$ is spatially modulated quasiperiodically with a strength ξ and frequency $\alpha = (\sqrt{5} + 1)/2$ (golden ratio), while the intracell coupling is kept fixed $J_{2,n} = J_2$. Here, ϕ is the phase of the quasiperiodic pattern.

In the case of an evanescently coupled waveguide array, the transport of optical fields is governed by the discrete Schrödinger equation [17, 18], $i\partial_z \psi = \hat{H}\psi$, where the propagation distance z plays the role of time, and ψ is a

* mukherjee@iisc.ac.in

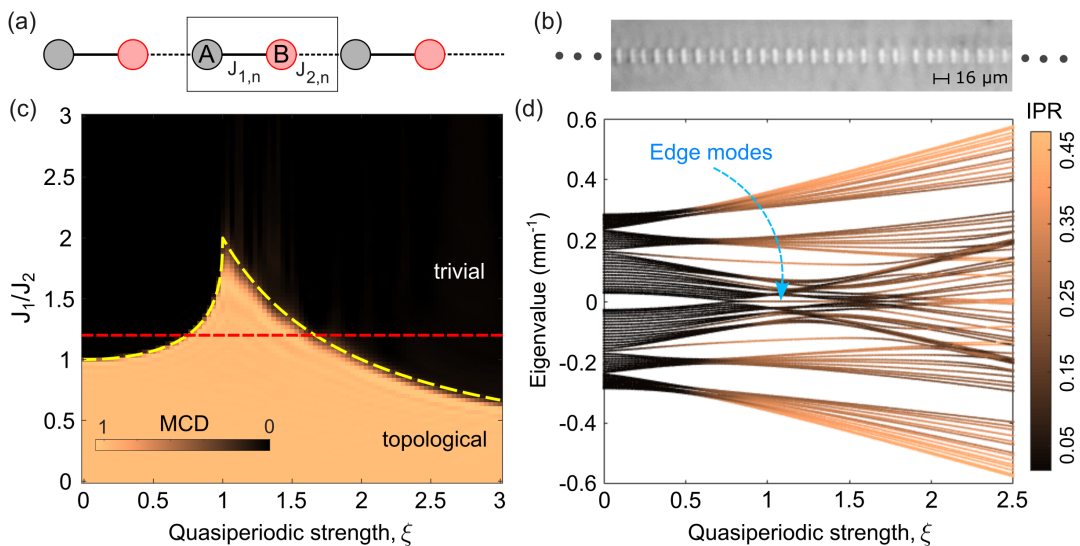


Figure 1. (a) Schematic of a one-dimensional lattice with fixed intra-cell couplings $J_{2,n}$ and quasiperiodic inter-cell couplings $J_{1,n}$. (b) Cross-sectional facet image of a femtosecond laser-written quasiperiodic lattice (30 out of a total of 80 sites are shown here). (c) Mean chiral displacement as a function of quasiperiodic strength ξ and the ratio of mean inter- to intra-cell couplings J_1/J_2 . The dashed yellow line indicates the phase boundary. (d) Energy spectrum as a function of quasiperiodic strength ξ for experimentally realized system sizes and $J_1/J_2 = 1.2$ [indicated by the dashed red line in (c)]. Zero-energy edge modes within the gap are visible for $0.75 < \xi < 1.67$. The color bar indicates the inverse participation ratio (IPR) of the eigenstates.

column vector whose elements are the peak amplitudes of the electric field of light at the lattice sites. By adjusting the inter-waveguide spacing, the desired couplings are realized in experiments.

In the absence of quasiperiodicity (i.e., $\xi = 0$), Eq. (1) describes a lattice with bipartite couplings; this is known as the Su-Schrieffer-Heeger model [47]. For $J_1 < J_2$, the SSH model possesses a non-trivial topology characterized by a non-zero topological invariant (called the Zak phase [48]) of the bulk bands, and the appearance of zero-energy edge modes for a finite system terminated with weak couplings at the two ends. Our model with $\xi \neq 0$ can exhibit interesting topological phases, as described below. Since disorder or quasiperiodicity breaks the translational symmetry of the system, the traditional topological invariants defined in the reciprocal k -space are not useful in our case. Additionally, many real-space variants [12, 16, 49] of such topological invariants depend on bulk eigenstates, making direct experimental observation challenging. To address this, we use the mean chiral displacement (MCD) [42–46], which converges to the winding number in the limit of a long propagation length. The chiral displacement is defined as

$$C(z) = \langle 2\Gamma X \rangle = 2 \sum_n n (|\psi_n^A|^2 - |\psi_n^B|^2), \quad (2)$$

where Γ is the chiral symmetry operator, X is the unit cell operator, and ψ_n^A (ψ_n^B) is the wave function at the A (B) site of the n -th unit cell. We initialize the input state at a single site of the 0-th unit cell at the middle of the lattice and record C as it evolves. Averaging the chiral displacement over a long propagation length L converges it to the *local winding number* (local with respect to the

input unit cell)

$$\bar{C} = \lim_{L \rightarrow \infty} \frac{1}{L} \int_0^L dz C(z). \quad (3)$$

In the case of disordered systems, further averaging over multiple input sites within the bulk, leading to $\langle \bar{C} \rangle$, reveals the topological invariant of the system in the limit of large system size [21, 49] (here, $\langle \rangle$ denotes the unit cell average).

Considering a large system size of 200 unit cells and a long propagation distance, we numerically obtain the mean chiral displacement as a function of ξ and J_1/J_2 , as shown in Fig. 1(c). In the absence of any disorder, the $J_1 < J_2$ ($J_1 > J_2$) region in Fig. 1(c) corresponds to the topologically non-trivial (trivial) phase of the SSH model. Upon introducing a quasiperiodic disorder, it is expected that, up to a certain disorder strength, the model should remain topologically non-trivial for $J_1 < J_2$. An interesting reentrant transition occurs in the $J_1 \gtrsim J_2$ region, where phase transitions from trivial to non-trivial and back to trivial occur as the quasiperiodic strength is increased. A specific case of $J_1/J_2 = 1.2$, indicated by the dashed red line in Fig. 1(c), is realized experimentally (see later). Considering the experimentally realized parameters, we plot the eigenvalues of the system with respect to the quasiperiodic strength ξ , as shown in Fig. 1(d). The spectrum is symmetric around the zero eigenvalue due to the chiral symmetry. In the clean case, we observe a band gap, but as ξ increases, the gap closes and reopens, signaling a topological phase transition. Specifically, for $0.75 < \xi < 1.67$, zero-energy topological modes emerge. Notably, the energy of these topological modes remains unchanged, and they

consistently appear as edge modes, even when we vary the frequency α (over irrational values) and phase ϕ of the quasiperiodic pattern. We analytically study the topological phase diagram by probing the zero-energy edge modes (Supplementary Material A) and confirm that the phase boundary is, in fact, independent of the choice of α (as long as it is irrational) and ϕ in the limit that the system is semi-infinite (i.e., the chain has one end). Indeed, by identifying the condition under which zero-energy edge modes can exist, we obtain the following analytical formula for the phase boundary, indicated by the dashed yellow line in Fig. 1(c),

$$\frac{J_1}{J_2} = \begin{cases} \frac{2}{1 + \sqrt{1 - \xi^2}} & \text{if } \xi \leq 1, \\ 2/\xi & \text{if } \xi > 1. \end{cases} \quad (4)$$

This result is elegant in the sense that J_2/J_1 (the inverse of Eq. (4)) is linear with ξ for $\xi > 1$ and forms a quarter ellipse for $\xi \leq 1$. The colorbar in Fig. 1(d) denotes the inverse participation ratio (IPR) of the eigenstates, which is defined as

$$\text{IPR} = \frac{\sum_n |\psi_n^A|^4 + |\psi_n^B|^4}{(\sum_n (|\psi_n^A|^2 + |\psi_n^B|^2))^2}, \quad (5)$$

where n ranges over the unit cell indices. The IPR is a measure of localization – it reaches unity when the wave function is localized to a single site. Note that the system primarily hosts delocalized eigenstates for small values of ξ ; see Fig. 1(d). As a function of the quasiperiodic strength, we observe three phases of delocalized, mixed and localized eigenstates; for details, see more Supplementary Material C. We also note that the spatial profile of the zero-energy edge modes in the TAI phase varies with ϕ . Since a single site initial state on the edge A site may not efficiently excite the edge modes, the measurement of $\langle \bar{C} \rangle$ is a natural experimental choice.

Wavelength Tuning.– The measurement of the mean chiral displacement requires probing intensity profiles as a function of z . In our experiments, the maximal propagation length of the photonic lattice is fixed, and measurements are often limited to the output intensities, although top imaging techniques have been employed in certain studies [50] to capture propagation dynamics in one-dimensional lattices. Here, we consider a wavelength-tuning technique that enables the extraction of the dynamics of light intensity by tuning the couplings with the wavelength λ of the incident light. The idea is straightforward to explain for a one-dimensional lattice with a homogeneous coupling J . In this case, when light is coupled at the 0-th site far away from the edges, the state at the n -th site is given by [51] $\psi_n(z) = (i)^n \mathcal{J}_n(2Jz)$, where \mathcal{J}_n is the n th-order Bessel function of the first kind. Evidently, the dynamics is determined by Jz , and hence, one can tune the wavelength of light to vary J , instead of z , to probe the dynamics.

The wavelength-tuning technique can be extended to the quasiperiodic lattice as long as the coupling ratios

$J_{1,n}/J_2$ remain wavelength-independent. We can express the Hamiltonian in Eq. (1) as $\hat{H} = J_2 \hat{H}'$, where \hat{H}' is independent of λ if $J_{1,n}/J_2$ does not change within the wavelength range of interest. In that case, the evolution operator is given by $\hat{U}(z) = \exp(-i\hat{H}'J_2z)$. Evidently, the propagation dynamics of the system is described by a normalized propagation distance J_2z . This approach leverages the fact that the output intensities remain identical for any combination of J_2 and z that yields the same value of J_2z .

Experiments.– The photonic devices are fabricated using the femtosecond laser writing technique [40, 41] in borosilicate (Corning Eagle XG) glass substrates. The inter-waveguide evanescent coupling is estimated by characterizing light transport in a set of two-waveguide devices. Experimental (black data points) and fitted variation of coupling with wavelength and inter-waveguide spacing d is shown in Fig. 2(a). The coupling varies linearly with λ and exponentially with d [52, 53]. By tuning the laser wavelength from 850 nm to 1050 nm, the normalized propagation distances can be varied from 3.8 to 12.7 in our experiments for a 76.2 mm-long device with a fixed inter-waveguide spacing of 16 μm . However, to minimize the deviation in the coupling ratios, we use a wavelength range of 100 nm in experiments, as described later. We note that the wavelength-tuning method also works for two-dimensional lattices where top imaging is more challenging.

To demonstrate the effectiveness of the wavelength-tuning method, we designed and fabricated 11 sets of SSH lattices, each consisting of 40 waveguides. For these lattices, we set $\xi = 0$, $J_2 = 0.072 \text{ mm}^{-1}$, and varied J_1 from 0.021 to 0.133 mm^{-1} . Horizontally polarized light was launched at a single A site of a unit cell in the bulk, and the output intensity patterns were measured within the wavelength range of 850 nm to 950 nm. The upper limit of $\lambda = 950 \text{ nm}$ is chosen so that the output state does not reach the edge of the lattice. In these bulk dynamics measurements, we can denote A (B) sites as B (A) sites and redefine the couplings, to obtain the MCD for both J_1/J_2 and its inverse from the same lattice. The chiral displacement, averaged over six independent measurements $\langle C(J_2z) \rangle$, is plotted in Fig. 2(b) for two different values of $J_1/J_2 = 0.77$ (red) and 1.42 (blue). The fluctuations in these measurements appear due to unavoidable small random disorder ($\Delta J/J \approx \pm 3\%$) in the lattices. The cumulative average of chiral displacement as a function of J_2z , $\langle \bar{C}(J_2z) \rangle$, for the two example coupling ratios is plotted in Fig. 2(c). The endpoints of this graph reveal the final MCD for the system. We then obtain the MCD as a function of J_1/J_2 ; this clearly shows a topological phase transition at $J_1/J_2 = 1$, see Fig. 2(d). We note that to experimentally obtain the MCD, we take the lower limit of the integration to be $\min[J_2z] = 3.76$ instead of zero.

To investigate bulk transport and topological phase transitions in our quasiperiodic model, we fabricated 12 sets of photonic lattices varying the quasiperiodic

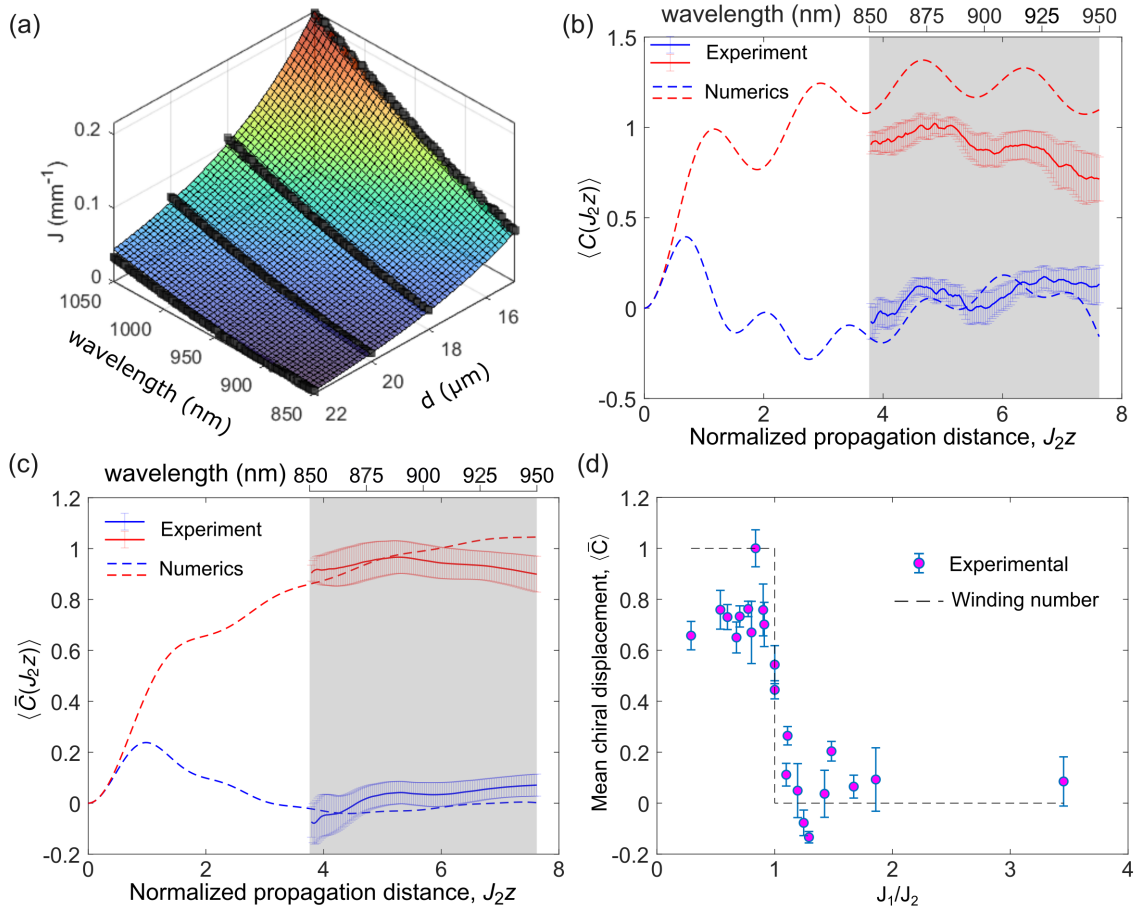


Figure 2. (a) Wavelength tuning: coupling strength J as a function of wavelength and inter-waveguide spacing d . Black squares denote the experimental data and the surface is its curvefit. (b) The chiral displacement $\langle C(J_{2z}) \rangle$, averaged over six independent measurements, for two different values of $J_1/J_2 = 0.77$ (red) and 1.42 (blue) (c) Cumulative average of chiral displacement as a function of J_{2z} , $\langle \bar{C}(J_{2z}) \rangle$, for $J_1/J_2 = 0.77$ (red) and 1.42 (blue). (d) Mean chiral displacement, $\langle \bar{C} \rangle$, as a function of J_1/J_2 for the SSH lattices showing a topological phase transition at $J_1/J_2 = 1$. The error bars in (b-d) are standard error of the mean value.

strengths from $\xi = 0.2$ to 2.4 . It is worth noting that the intercell coupling $J_{1,n}$ can become negative for higher values of ξ ; however, we can gauge out the negative couplings and effectively work with $|J_{1,n}|$, which is feasible for fabrication. Indeed, in a one-dimensional tight-binding model, altering the phases of the coupling constants does not impact the physical observables of the system; see Supplementary Material B. Figure 3(a) presents the quasiperiodic couplings realized in the experiment with $\xi = 0.8$ at 950 nm wavelength. We calculate the chiral displacement $C(J_{2z})$ from the extracted dynamics to assess the topological properties. For instance, Figs. 3(b-d) present $C(J_{2z})$ as a function of the wavelength (or J_{2z}) for three values of $\xi = 0.2, 0.9$, and 2 , respectively; the different colors are associated with ten measurements by coupling light at ten different input sites. In these experiments, the average variation of $J_{1,n}/J_2$ is found to be less than 5% from its mean value, for a wavelength span of $\lambda = 1000 \pm 50$ nm. By averaging over the input sites and the normalized propagation distance, we calculate the mean chiral displacement

$\langle \bar{C}(J_{2z}) \rangle$, as shown in Fig. 3(e). For $\xi < 0.75$ and $\xi > 1.67$, the value of $\langle \bar{C}(J_{2z}) \rangle$ was measured to be less than 0.35 . However, we observe a significant increase in the MCD values within the range of $0.75 < \xi < 1.67$; this indicates a topological phase transition from trivial to non-trivial and back to trivial.

The agreement between experimental and theoretical results validates our approach and demonstrate the feasibility of probing topological properties through wavelength tuning in photonic lattices. The precision of our results could be further enhanced by employing a longer sample with more lattice sites, which would allow for an extended range of normalized propagation distances accessible via wavelength tuning. It should be noted that the presence of random disorder in the on-site energy and a next-nearest-neighbor coupling can destroy the chiral symmetry. However, these effects are insignificant in our experiments and do not significantly affect the measurement of the MCD.

Conclusions.— We have experimentally and numerically studied light transport in the bulk of a quasi-

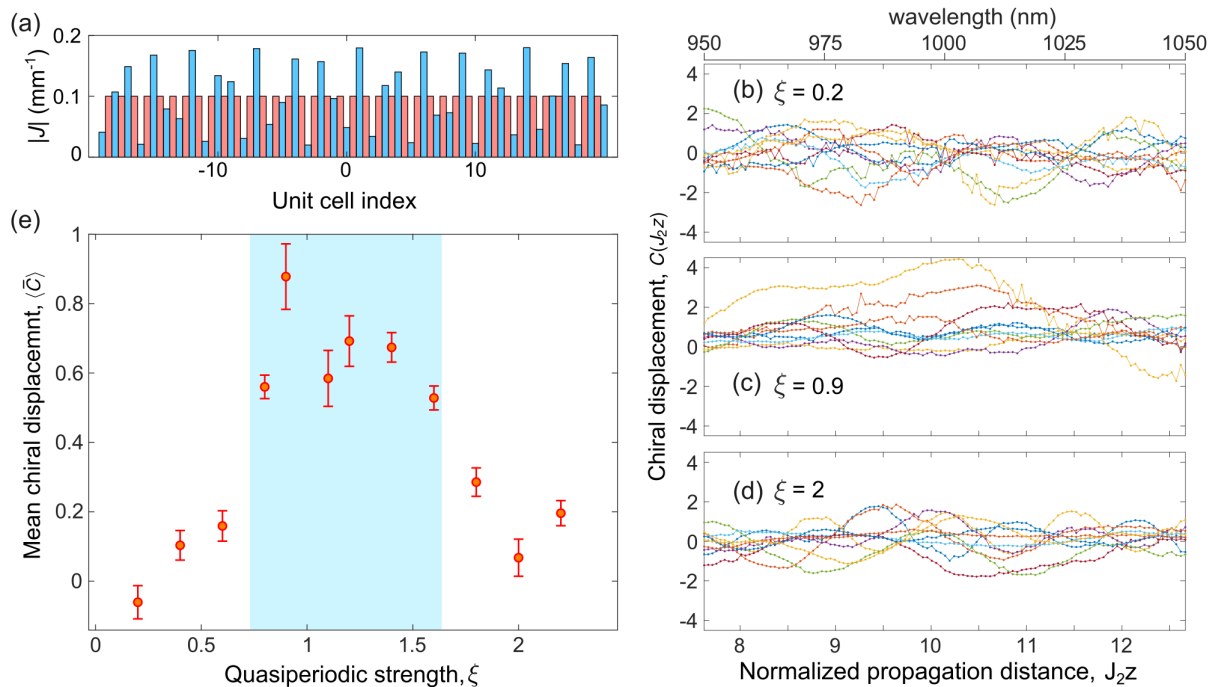


Figure 3. (a) Experimentally realized quasiperiodic couplings. Here, red (blue) color indicates $J_{1,n}$ ($J_{2,n}$) at 950 nm wavelength of light. (b-d) Experimentally obtained chiral displacements $C(J_{2z})$ as a function of wavelength (or, J_{2z}) for quasiperiodic strengths $\xi = 0.2$, $\xi = 0.9$ and $\xi = 2$, respectively. Different coloured lines represent different initial excitation at different input sites. (e) Mean chiral displacement as a function of ξ . Red circles are experimental data points with error bars denoting the standard error of the mean value of $\langle C(J_{2z}) \rangle$. The shaded region corresponds to the topologically non-trivial phase.

periodic photonic SSH lattice. By recording the output intensity patterns as a function of the wavelength of light, we determine the mean chiral displacement that captures the topological features of the system. Importantly, we demonstrate a reentrant transition from a trivial to topological and back to a trivial phase as a function of the quasiperiodic strength. Our results provide key insights into the physics of topology and quasiperiodic disorder and showcase the versatility of photonic lattices as a platform for topological studies. Additionally, it should be noted that laser-fabricated photonic lattices are a natural platform to realize Floquet topological materials and study the influence of self-focusing Kerr nonlinearity using intense laser pulses [54–56]. Evidently, our results will be useful for further exploring the interplay of periodic driving, topology, disorder and nonlinear interactions.

Acknowledgments.— We thank Ferdinand Evers and Tapan Mishra for useful discussions. S.M. gratefully acknowledges support from the Indian Institute of Science (IISc) for funding through a start-up grant, the Ministry of Education, Government of India, for funding through STARS (MoESTARS/STARS-2/2023-0716) and the Infosys Foundation, Bangalore. T.S. and A.T. thank IISc and CSIR, respectively, for their Ph.D. scholarships. D.S. thanks SERB, India, for funding through Project No. JBR/2020/000043. We sincerely thank Nicholas Smith of Corning Inc. for providing high-quality glass wafers.

Supplementary Material

In the following sections of the supplementary material, we present experimental and numerical results for completeness.

A. Topological phase diagram

Figure 1(c) in the main text shows the mean chiral displacement as a function of J_1/J_2 and ξ . Here, we derive an analytical expression for the phase boundary. Our goal is to identify the condition under which zero-energy edge modes can exist, as the topological phase with the correct termination can support such modes. For the quasiperiodic SSH lattice, we have the following equations in the site basis for an eigenmode with energy E ,

$$E\psi_n^A = J_2\psi_{n-1}^B + J_{1,n}\psi_n^B, \quad (\text{A1})$$

$$E\psi_n^B = J_{1,n}\psi_n^A + J_2\psi_{n+1}^A. \quad (\text{A2})$$

Unlike the main text, we will consider here a semi-infinite lattice, where the unit cell index n varies from 1 to infinity. For the zero-energy eigenstate, Eqs. (A1, A2) imply that

$$\psi_n^A = (-1)^{n-1} \frac{\prod_{i=1}^{n-1} J_{1,i}}{J_2^{n-1}} \psi_1^A, \quad (\text{A3})$$

$$\psi_n^B = 0. \quad (\text{A4})$$

This shows that for $E = 0$, the amplitudes on all the B -sites vanish, while the A -site amplitudes follow a recursion relation leading them to be proportional to the amplitude on edge A site, ψ_1^A . For a state localized near the edge, the amplitude must decay as $n \rightarrow \infty$, leading to the condition

$$\frac{\prod_{n=1}^N J_{1,n}}{J_2^N} < 1 \quad \text{as } N \rightarrow \infty, \quad (\text{A5})$$

where the total number of sites is $2N$. Substituting the couplings $J_{1,n}$ and $J_{2,n}$ in Eq. (A5), we obtain the phase diagram presented in Fig. A1, which is in excellent agreement with Fig. 1(c). This reinforces the fact that the topological phase reported using mean chiral displacement corresponds to zero-energy edge modes.

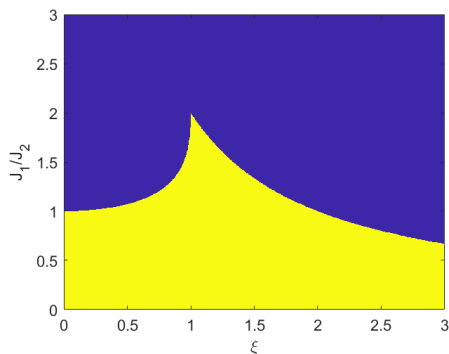


Figure A1. Topological phase diagram for a large system size of 2000 unit cells. The yellow region satisfies the condition (A5).

For the quasiperiodic pattern considered here, we now show that the shape of the phase boundary is independent of the choice of the irrational number α and the phase ϕ for a very large system size. The phase boundary satisfies the following critical condition

$$\frac{\prod_{n=1}^N J_{1,n}}{J_2^N} = 1, \quad (\text{A6})$$

which implies

$$\frac{1}{N} \sum_{n=1}^N \log |1 + \xi \cos(2\pi\alpha n + \phi)| = \log \left(\frac{J_2}{J_1} \right). \quad (\text{A7})$$

Note that the term $(2\pi\alpha n + \phi) \pmod{2\pi}$ uniformly samples all the points in $[0, 2\pi]$ as $N \rightarrow \infty$, because of the *irrationality* of α . This allows us to convert the sum in the LHS of Eq. (A7) to an integral,

$$\log \left(\frac{J_2}{J_1} \right) = \int_0^1 dx \log |1 + \xi \cos(2\pi x)|. \quad (\text{A8})$$

The integral can be evaluated using complex variables and yields the expression

$$\frac{J_1}{J_2} = \begin{cases} \frac{2}{1 + \sqrt{1 - \xi^2}} & \text{if } \xi \leq 1, \\ 2/\xi & \text{if } \xi > 1. \end{cases} \quad (\text{A9})$$

Eq. (A9) accurately describes the phase boundary and, notably, is independent of the choice of phase ϕ and α as long as it is irrational. The dashed yellow curve in Fig. 1(c) corresponds to the phase boundary defined by this equation.

B. Gauging out negative couplings

In this section, we will explain the transformation which allows us to take the absolute value of the couplings to eliminate negative values. Consider a general one-dimensional tight-binding model

$$H = - \sum_n [t_n \hat{c}_n^\dagger \hat{c}_{n+1} + \text{H.c.}], \quad (\text{A10})$$

where t_n is the coupling constant, and \hat{c}_n represents the annihilation operator at site n . Now, suppose that we change the phase of any particular coupling

$$t_j \rightarrow t_j \exp(i\theta). \quad (\text{A11})$$

We can then apply either of the following transformations

$$c_{j'} \rightarrow c_{j'} \exp(i\theta) \quad \text{for all } j' \leq j, \quad (\text{A12})$$

$$\text{or } c_{j'} \rightarrow c_{j'} \exp(-i\theta) \quad \text{for all } j' \geq j+1, \quad (\text{A13})$$

to remove the phase θ from t_j , while keeping the Hamiltonian unchanged. Thus, these transformations allow negative values of couplings to be gauged out, enabling us to work with the absolute values of the couplings in experiments.

C. Localization properties of the quasiperiodic model

In this section, we analyze the localization properties of the eigenstates in our quasiperiodic model for a fixed coupling ratio given by $J_1/J_2 = 1.2$. In addition to the observed topological transitions, the system undergoes a localization transition, which we characterize using the inverse participation ratio (IPR). Our results reveal three distinct phases: delocalized, mixed, and fully localized states (Fig. A2).

For quasiperiodic strength $\xi \lesssim 0.5$, the system primarily hosts delocalized eigenstates. Beyond this, in the range $0.5 \lesssim \xi \lesssim 1.75$, the eigenstates exhibit a coexistence of localized and delocalized characteristics, forming a mixed phase. When $\xi \gtrsim 1.75$, the system fully transitions into a localized phase, where all eigenstates are confined with $\text{IPR} \gtrsim 0.1$.

D. Fabrication and characterization details

In this section, we briefly discuss how the photonic lattices were fabricated and characterized. All waveguide-based photonic devices were created using femtosecond laser writing [40, 41] – a laser-based technique that induces refractive index modifications within a transparent

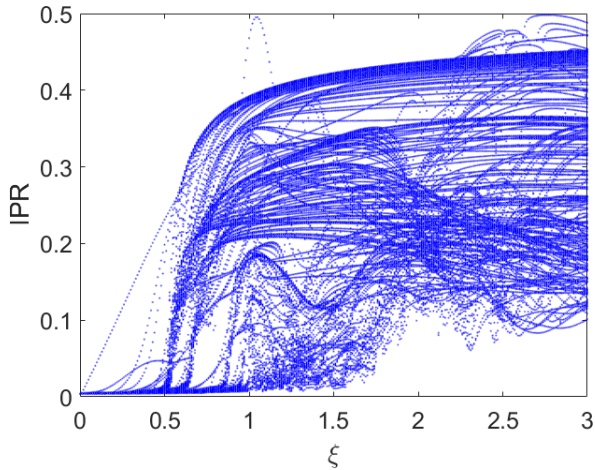


Figure A2. IPRs of the eigenstates of the quasiperiodic model for $J_1/J_2 = 1.2$.

dielectric medium. We use a Yb-doped fiber laser system (Satsuma, Amplitude) to generate 260 fs optical pulse trains with 500 kHz repetition rate and 1030 nm central wavelength. To regulate the power and polarization of the laser beam, we utilized a polarizing beam splitter and wave plates. The laser beam with circular polarization is focused (using a 0.4 NA lens) within a Corning Eagle XG glass substrate mounted on high-precision x - y - z translation stages (Aerotech Inc). Each waveguide is created by translating the substrate once through the focus of the laser beam at a speed of 6 mm/s and an average laser power of 170 mW.

The photonic devices were characterized using a wavelength tunable super-continuum source (NKT Photonics). We focused the light at a single desired waveguide at the input and imaged the output intensity pattern on a CMOS camera. For broadband performance, we used achromatic doublet lenses. We used horizontally polarized light for all characterization experiments.

-
- [1] K. v. Klitzing, G. Dorda, and M. Pepper, *Physical Review Letters* **45**, 494 (1980).
- [2] D. J. Thouless, M. Kohmoto, M. P. Nightingale, and M. den Nijs, *Physical Review Letters* **49**, 405 (1982).
- [3] T. Ozawa, H. M. Price, A. Amo, N. Goldman, M. Hafezi, L. Lu, M. C. Rechtsman, D. Schuster, J. Simon, O. Zilberberg, *et al.*, *Reviews of Modern Physics* **91**, 015006 (2019).
- [4] M. C. Rechtsman, J. M. Zeuner, Y. Plotnik, Y. Lumer, D. Podolsky, F. Dreisow, S. Nolte, M. Segev, and A. Szameit, *Nature* **496**, 196 (2013).
- [5] J. Li, R.-L. Chu, J. K. Jain, and S.-Q. Shen, *Physical Review Letters* **102**, 136806 (2009).
- [6] P. Titum, N. H. Lindner, M. C. Rechtsman, and G. Refael, *Physical Review Letters* **114**, 056801 (2015).
- [7] A. Agarwala and V. B. Shenoy, *Physical Review Letters* **118**, 236402 (2017).
- [8] C. Groth, M. Wimmer, A. Akhmerov, J. Tworzydło, and C. Beenakker, *Physical Review Letters* **103**, 196805 (2009).
- [9] E. Prodan, *Journal of Physics A: Mathematical and Theoretical* **44**, 239601 (2011).
- [10] L. Chen, Q. Liu, X. Lin, X. Zhang, and X. Jiang, *New Journal of Physics* **14**, 043028 (2012).
- [11] J. Song and E. Prodan, *Physical Review B* **89**, 224203 (2014).
- [12] I. Mondragon-Shem, T. L. Hughes, J. Song, and E. Prodan, *Physical Review Letters* **113**, 046802 (2014).
- [13] H.-C. Hsu and T.-W. Chen, *Physical Review B* **102**, 205425 (2020).
- [14] L. Lin, S. Kruk, Y. Ke, C. Lee, and Y. Kivshar, *Physical Review Research* **2**, 043233 (2020).
- [15] D.-W. Zhang, L.-Z. Tang, L.-J. Lang, H. Yan, and S.-L. Zhu, *Science China Physics, Mechanics & Astronomy* **63**, 267062 (2020).
- [16] L. Lin, Y. Ke, and C. Lee, *Physical Review B* **103**, 224208 (2021).
- [17] D. N. Christodoulides, F. Lederer, and Y. Silberberg, *Nature* **424**, 817 (2003).
- [18] I. L. Garanovich, S. Longhi, A. A. Sukhorukov, and Y. S. Kivshar, *Physics Reports* **518**, 1 (2012).
- [19] I. Bloch, J. Dalibard, and S. Nascimbene, *Nature Physics* **8**, 267 (2012).
- [20] S. Stützer, Y. Plotnik, Y. Lumer, P. Titum, N. H. Lindner, M. Segev, M. C. Rechtsman, and A. Szameit, *Nature* **560**, 461 (2018).
- [21] E. J. Meier, F. A. An, A. Dauphin, M. Maffei, P. Massignan, T. L. Hughes, and B. Gadway, *Science* **362**, 929 (2018).
- [22] M. Ren, Y. Yu, B. Wu, X. Qi, Y. Wang, X. Yao, J. Ren, Z. Guo, H. Jiang, H. Chen, *et al.*, *Physical Review Letters* **132**, 066602 (2024).
- [23] P. W. Anderson, *Physical Review* **109**, 1492 (1958).
- [24] P. A. Lee and T. V. Ramakrishnan, *Reviews of Modern Physics* **57**, 287 (1985).
- [25] T. Schwartz, G. Bartal, S. Fishman, and M. Segev, *Nature* **446**, 52 (2007).
- [26] S. Aubry and G. André, *Ann. Israel Phys. Soc* **3**, 18 (1980).
- [27] Y. Lahini, R. Pugatch, F. Pozzi, M. Sorel, R. Morandotti, N. Davidson, and Y. Silberberg, *Physical Review Letters* **103**, 013901 (2009).
- [28] Y. E. Kraus, Y. Lahini, Z. Ringel, M. Verbin, and O. Zilberberg, *Physical Review Letters* **109**, 106402 (2012).
- [29] S. Ganesan, J. Pixley, and S. Das Sarma, *Physical Review Letters* **114**, 146601 (2015).
- [30] S. Roy, T. Mishra, B. Tanatar, and S. Basu, *Physical Review Letters* **126**, 106803 (2021).
- [31] S. Aditya, K. Sengupta, and D. Sen, *Phys. Rev. B* **107**, 035402 (2023).
- [32] J. Song, H. Liu, H. Jiang, Q.-F. Sun, and X. Xie, *Physical Review B—Condensed Matter and Materials Physics* **85**, 195125 (2012).

- [33] A. Girschik, F. Libisch, and S. Rotter, *Physical Review B—Condensed Matter and Materials Physics* **88**, 014201 (2013).
- [34] Y. Kuno, *Physical Review B* **100**, 054108 (2019).
- [35] L.-Z. Tang, S.-N. Liu, G.-Q. Zhang, and D.-W. Zhang, *Physical Review A* **105**, 063327 (2022).
- [36] S. Nakajima, N. Takei, K. Sakuma, Y. Kuno, P. Marra, and Y. Takahashi, *Nature Physics* **17**, 844 (2021).
- [37] S. Longhi, *Optics Letters* **45**, 4036 (2020).
- [38] J. Gao, Z.-S. Xu, D. A. Smirnova, D. Leykam, S. Gyger, W.-H. Zhou, S. Steinhauer, V. Zwiller, and A. W. Elshaari, *Physical Review Research* **4**, 033222 (2022).
- [39] W. Cheng, W. Liu, Q. Liu, and F. Chen, *Optics Letters* **47**, 2883 (2022).
- [40] K. M. Davis, K. Miura, N. Sugimoto, and K. Hirao, *Optics Letters* **21**, 1729 (1996).
- [41] A. Szameit and S. Nolte, *Journal of Physics B: Atomic, Molecular and Optical Physics* **43**, 163001 (2010).
- [42] F. Cardano, A. D’Errico, A. Dauphin, M. Maffei, B. Piccirillo, C. de Lisio, G. De Filippis, V. Cataudella, E. Santamato, L. Marrucci, *et al.*, *Nature Communications* **8**, 15516 (2017).
- [43] M. Maffei, A. Dauphin, F. Cardano, M. Lewenstein, and P. Massignan, *New Journal of Physics* **20**, 013023 (2018).
- [44] S. Longhi, *Optics Letters* **43**, 4639 (2018).
- [45] A. D’Errico, F. Di Colandrea, R. Barboza, A. Dauphin, M. Lewenstein, P. Massignan, L. Marrucci, and F. Cardano, *Physical Review Research* **2**, 023119 (2020).
- [46] N. Roberts, G. Baardink, J. Nunn, P. J. Mosley, and A. Souslov, *Science Advances* **8**, eadd3522 (2022).
- [47] W.-P. Su, J. R. Schrieffer, and A. J. Heeger, *Physical Review Letters* **42**, 1698 (1979).
- [48] M. Atala, M. Aidelsburger, J. T. Barreiro, D. Abanin, T. Kitagawa, E. Demler, and I. Bloch, *Nature Physics* **9**, 795 (2013).
- [49] R. Bianco and R. Resta, *Physical Review B—Condensed Matter and Materials Physics* **84**, 241106 (2011).
- [50] A. Szameit, F. Dreisow, H. Hartung, S. Nolte, A. Tünnermann, and F. Lederer, *Applied Physics Letters* **90**, 10.1063/1.2735953 (2007).
- [51] A. L. Jones, *Journal of the Optical Society of America* **55**, 261 (1965).
- [52] A. Szameit, F. Dreisow, T. Pertsch, S. Nolte, and A. Tünnermann, *Optics express* **15**, 1579 (2007).
- [53] S. Mukherjee, D. Mogilevtsev, G. Y. Slepyan, T. H. Doherty, R. R. Thomson, and N. Korolkova, *Nature Communications* **8**, 1909 (2017).
- [54] S. Mukherjee and M. C. Rechtsman, *Science* **368**, 856 (2020).
- [55] H. Eisenberg, Y. Silberberg, R. Morandotti, A. Boyd, and J. Aitchison, *Physical Review Letters* **81**, 3383 (1998).
- [56] T. Shit, R. Hui, M. Di Liberto, D. Sen, and S. Mukherjee, arXiv:2402.18340 [10.48550/arXiv.2402.18340](https://arxiv.org/abs/10.48550/arXiv.2402.18340) (2024).